Polymer nano manufacturing of a biomimicking surface for kidney stone crystallization studies

Pleeging, R.M.B.; Ibis, F.; Fan, D.; Sasso, L.; Eral, H.B.; Staufer, U.

DOI
10.1016/j.mne.2021.100094

Publication date
2021

Document Version
Final published version

Published in
Micro and Nano Engineering

MNE 13 (2021) 100094

Contents lists available at ScienceDirect

Micro and Nano Engineering

journal homepage: www.sciencedirect.com/journal/micro-and-nano-engineering

Polymer nano manufacturing of a biomimicking surface for kidney stone crystallization studies

R.M.B. Pleeging [a], F. Ibis [b], D. Fan [a], L. Sasso [a], H.B. Eral [b], U. Staufer [a,*]

[a] Delft University of Technology, Dept. of Precision and Microsystems Engineering, Delft 2628CD, the Netherlands
[b] Delft University of Technology, Dept. of Process and Energy, Delft 2628CD, the Netherlands

ARTICLE INFO

Keywords:
Kidney stones
Two-photon polymerization
Biomimicry
Organ-on-a-chip

ABSTRACT

Detected kidney stone cases are increasing globally, yet knowledge on the conditions for stone formation is lacking. Experimental approaches mimicking the micro-environmental conditions present in vivo can help scientists untangle intertwined physiochemical and biological phenomena leading to kidney stone formation. As crystal nucleation often initiates at liquid-solid interfaces, the interface morphology plays a significant role in the rate of nucleation. Within the nephron, the functional unit of the kidney, four segments can be distinguished that contain different surface morphologies. Particularly, the cells lining these segments contain protrusions in the shape of nanopillars that vary in length, diameter and spacing. Exploiting the opportunities provided by organ-on-a-chip technology, we designed and manufactured a proof-of-principle microfluidic device proposed to increase our understanding of the relation between kidney surface morphology and kidney stone crystallization. We used two-photon polymerization to fabricate biocompatible surfaces that mimic the nephron morphologies with materials properties similar to those of biological structures. The fabricated cilia were incorporated in the microfluidic device, which was designed to observe in vitro crystallization of calcium oxalate under flow.

1. Introduction

Kidney stone disease has an increasing prevalence world-wide [1] and costs the private sector about five billion dollars annually [2]. The disease has plagued humanity for several millennia [3,4] and a great deal of knowledge on stone growth has been acquired by biopsies and examination of removed stones. Yet this approach provides only information after the stone was formed. Consequently, the exact mechanisms that drive stone formation, particularly for most commonly encountered calcium oxalate stones are still lacking. The lack of experimental instrumentation mimicking the kidney's micro-environmental conditions in vivo, has only recently been filled by the emergence of microfluidics and organ-on-a-chip technologies. These technologies provide us an opportunity to study the formation of kidney stones in vitro. A recent study has tried to capture some of the physiological conditions of the kidney in a biomimetic model in order to study the crystallization of calcium oxalate (CaOx) [5]. In that study, Laffite et al. proposed a microfluidic channel with dimensions matching the collecting duct of the human kidney, using physiological concentrations and flow rates. Crystallization is however a stochastic process influenced by thermodynamics and kinetic factors, amongst which the surface characteristics of the solid-liquid interface plays a critical role [6]. Similarly, a recent study showed that the surface morphology of the interface can promote or hinder nucleation of crystals [7]. Within the nephron, the functional unit of the kidney, four separate segments can be distinguished that contain different surface morphologies: the proximal convoluted tubule (PCT), the thin segments of the Loop of Henle (LoH), the distal convoluted tubule (DCT) and the collecting duct (CD). Particularly, the cells lining these segments contain micro-projections called microvilli and cilia, shaped as nanopillars that vary in diameter (d), height (h) and spacing (s). The relation between nephron surface morphology and kidney stone formation has to our knowledge not yet been studied, although rough surfaces can induce heterogeneous crystallization in general [8,9]. Further, studies have related increased kidney stone crystal attachment to cell surface morphology and cell health [10,11]. Though there are multiple pathways where local supersaturation can initialize kidney stone nucleation and subsequent grown in the complex solution chemistry of urine [12–14], by isolating different physical and chemical properties of the nephron a better understanding of some of these pathways can be developed. For example Randall's plaque in the LoH can initiate crystal formation, what then is the role of the microstructure of downstream segments in crystal growth and consolidation?

* Corresponding author.
E-mail address: u.staufer@tudelft.nl (U. Staufer).

https://doi.org/10.1016/j.mne.2021.100094
Received 13 July 2021; Received in revised form 24 August 2021; Accepted 25 August 2021
Available online 28 August 2021

Table 1
Renal micro-projection typical dimensions where d is the diameter, h is the height, s is the spacing between micro-projections.

Segment	Type of protrusion	*d* [nm]	*h* [μm]	s [nm]
PCT	brush border of microvilli [22]	80 [22]	1–2 [23]	75–130 [24,25]
LoH	none [22]	–	–	–
DCT	sparse microvilli [22]	80 [22]	<0.5 [26,27]	varying [26,29,30]
CD	primary cilium [22]	250 [22]	2–10 [23,28]	≈ 8′000 [31,32]
CD	brush border of microvilli [22]	80 [22]	<0.5 [26,27]	75–130 [24,25]

Alternatively, how does surface morphology affect local flow patterns and thus free solution crystallization?

Here we propose an approach to fabricate polymer nanopillar arrays, using two-photon polymerization (2PP), in order to mimic the surface morphology of the different nephron segments. Such pillars which mimic the nephron morphology may induce heterogeneous nucleation, leading to more kidney stones. This fabrication method can encompass the large dimensional variety that micro-projections possess and does not involve complicated fabrication steps. Multiple channels with different micro-structures and smooth channels can be printed on the same device, allowing comparison, statistical studies, and isolation of specific micro-structures. 2PP exploits the non-linear dependency of a material's two-photon absorption rate on the incident light intensity [15]. This causes the polymerization to occur only within a very small, central region surrounding the focal point [16,17]. By directing this region along a 3D path through photoresin, the technique can be used for 3D direct laser writing. The photoresin used is an acrylate based polymer with similar mechanical properties to the kidney micro-projections: an elastic modulus of ~2 GPa [17] compared to ~1 GPa of actin, and a flexural modulus of ~0.3 GPa (supplementary information) compared to the ~0.1 GPa of microvillum [18–21].

1.1. Renal micro-projections: cilia and microvilli

Renal microvilli typically are about 80 nm in diameter [22] and 1–2 μm in height [23] for a well-developed brush border. The spacing between microvilli varies with the flow rate in the tubule, and is about 75 to 130 nm in the brush border [24,25]. Microvilli can also appear as small bumps on the cell surface [26] having a relatively short length of 500 nm or less [27]. The cilium is much larger, having a diameter of about 250 nm [22] and a height of 2–10 μm [23,28]. The Young's modulus of both the microvillus and cilium has been measured to be in the order of about 1 GPa while the flexural modulus is approximately 0.1 GPa [18–21]. The dimensions of the cilia and microvilli are summarized in Table 1.

The micro-projections found on the cell membranes in the different segments of the nephron were approximated as nanopillars with the above characteristic dimensions. To mimic these micro-projections using 2PP, we first tested the mechanical properties of the photoresin using micro-mechanical testing to ensure the flexural modulus resembles that of the microvilli and cilia. We then aimed to write nanopillars with i) d = 80 nm, h = 1 μm, s = 120 nm, and ii) d = 250 nm, h = 8 μm, s = 8000 nm, representing the microvilli and cilia respectively in terms of geometry. Then, using standard soft lithography, a proof-of-principle microfluidic organ-on-a-chip was fabricated, into which the written nanopillars were incorporated and finally used to crystallize CaOx.

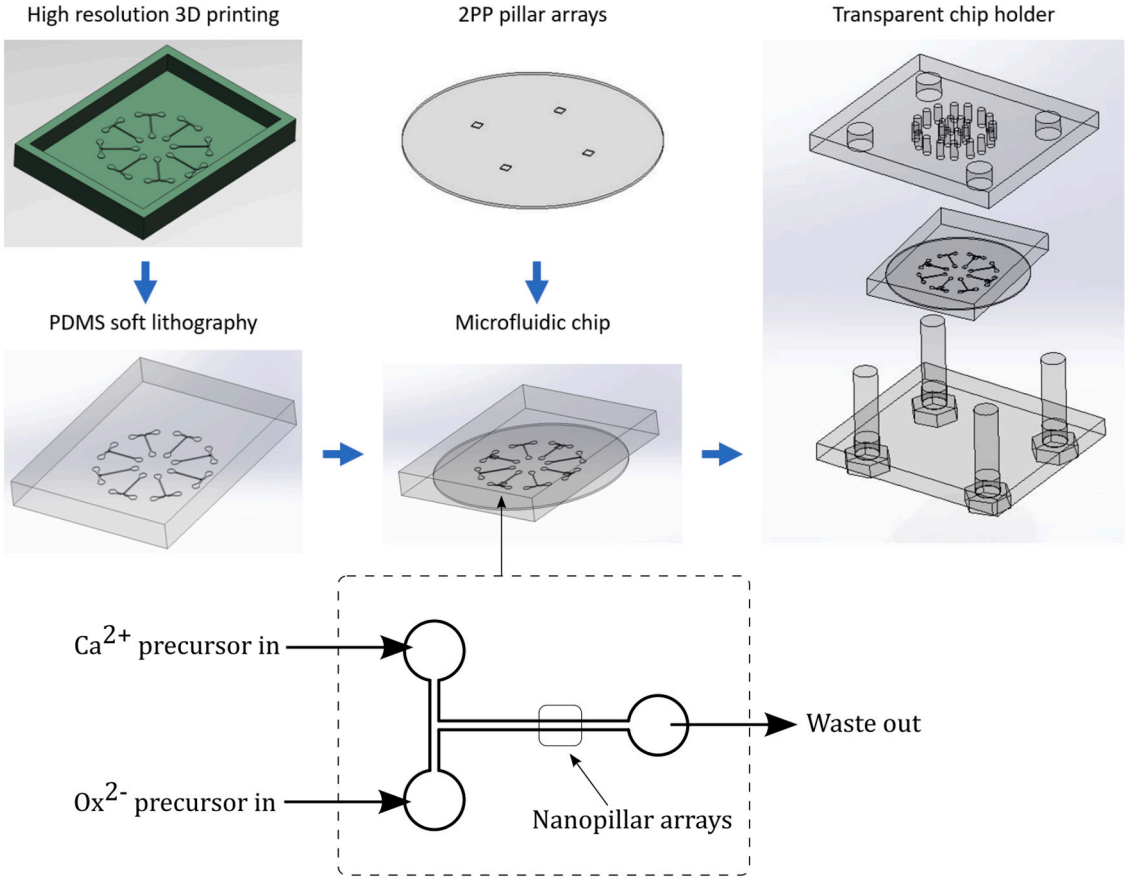

Fig. 1. Fabrication steps of the microfluidic device (top). Schematic of microfluidic device (bottom).

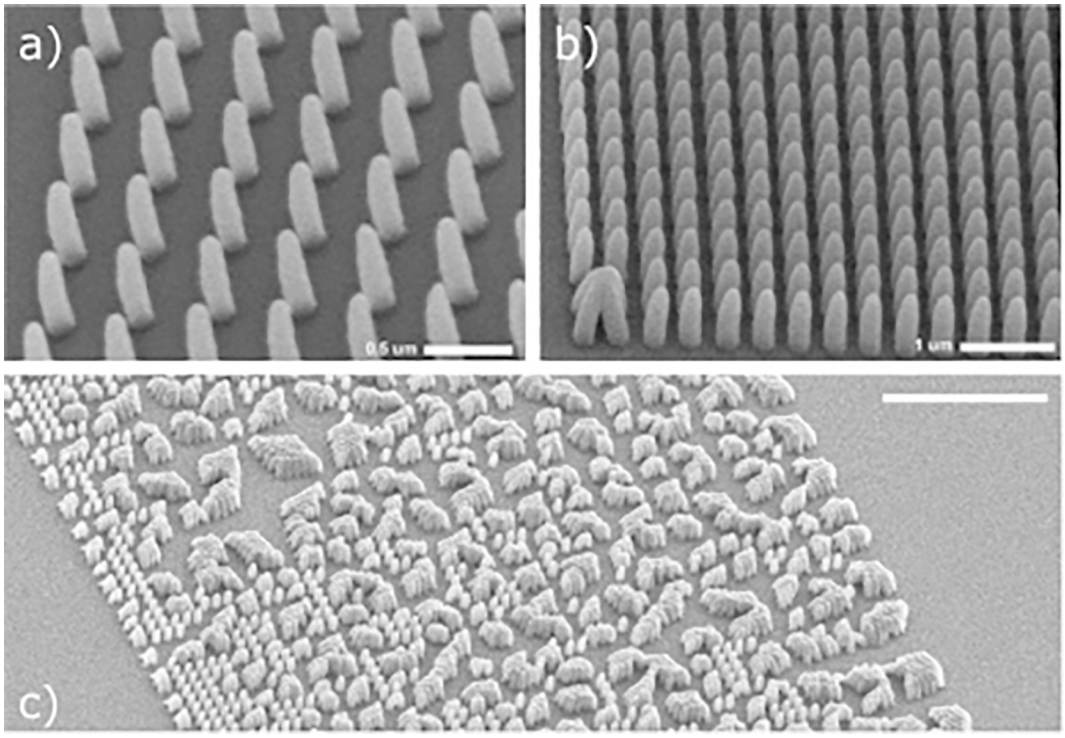

Fig. 2. SEM images of the written nanopillar samples on a 45° sample holder, showing a) minimum pillar diameter of 145 nm ± 4 nm (with height of 692 ± 8 nm and spacing of 355 ± 4 nm), b) minimum pillar-to-pillar spacing of 157 nm ± 8 nm (with height of 692 ± 8 nm and diameter of 243 ± 8 nm), c) pillar arrays without post-processing using critical point drying showing pillar collapse due to surface tension forces during drying. Scale bars are in: a) 0.5 μ*m,* b) 1 μ*m,* c) 5 μ*m.*

2. Experimental

2.1. 2PP fabrication

Nanopillars were fabricated with the Photonic Professional GT (Nanoscribe GmbH) in both conventional and dip-in mode with an objective lens of 63× magnification and numerical aperture of 1.4. First, a glass coverslip (Menzel-Gläser) with diameter 30 mm and thickness 0.17 mm +/− 0.01 mm was rinsed with acetone (Merck KGaA) and wiped with a soft cloth. The coverslip was then rinsed with 2-propanol (IPA, Honeywell Riedel-de-Haën) and again wiped with a soft cloth. The coverslip was placed on the sample holder and fastened with adhesive tape (Nanoscribe GmbH). On the bottom of the coverslip a droplet of immersion oil (Immersol 518 F, Zeiss) was placed, and on the top a droplet of negative tone photo-resist IP-L 780 (Nanoscribe GmbH) for conventional mode operation. For dip-in mode, a droplet of IP-Dip (Nanoscribe GmbH) was placed on the bottom of the coverslip alone. A customized script was used to write pillar arrays layer-by-layer with different laser power for each layer along the axis of the pillars. By changing the laser power throughout the length of a pillar, the shape of that pillar could be manipulated. Both laser power and scan speed were varied to optimize for the correct nanopillar size. Further, since the specified resolution limit of the tool is 200 nm in the x-y plane, to achieve a pillar diameter of 100 nm the designed pillars were undersized to a diameter of 10 nm and over-dosed by adjusting the laser power and scan speed accordingly to the target size. This means the pillar diameter is adjusted not by moving the voxel in space, but by using high laser power to cause voxel growth [33]. Similar resolution structures have been fabricated by using custom photoresins [34,35] and oxygen scavenging additives [36,37]. Nanopillars were also written with multiple passes over the same volume to better control local laser heating and subsequently the polymerization process. Finally, scanning with galvo mirror, where the writing direction is generally swept in the x-y plane, versus moving the piezo stage in the z writing direction was compared.

After writing, the coverslip was placed in a custom-made holder and immersed for 25 min in propylene glycol monomethyl ether acetate (PGMEA, Sigma-Aldrich) for development, followed by an immersion for 5 min in IPA for rinsing. A critical point dryer (Emitech K850) was used to circumvent surface tension when drying the developed structure after removing from IPA. The capillary forces caused by the surface tension of the rinsing liquid during air-drying would have caused the pillars to collapse otherwise.

Finally, test structures of singly clamped beams of length 45 μm, width 5 μm, and height 5 μm were fabricated from IP-Dip and the flexural modulus of the material measured using a micro-mechanical testing tool (FT-NMT03, FemtoTools AG). The details of these measurements are provided in Supplementary Information.

2.2. Characterization

To inspect and measure the dimensions of the written pillars, the coverslip with the structures was sputter coated (SC7620, Quorum Technologies) with a 6 nm layer of gold/palladium (Au/Pd) and imaged in a scanning electron microscope (SEM, Jeol JSM-6010LA) using a 45° sample holder. Measurements were made to calculate the mean diameter and its standard deviation (SD) using image analysis software (ImageJ). In this paper, SD is indicated with a ± value. The spacing in between two pillars was calculated using the predetermined center-to-center spacing and the measured mean diameter.

2.3. Manufacturing the microfluidic device

The fabrication steps of the microfluidic device are summarized in Fig. 1. High-resolution 3D printing (Envision TEC Micro Plus Hi-res) was used to fabricate a mold master from photo-curable resin (HTM140, Envision TEC). The mold master contained the negative versions of eight 100 μm high and 150 μm wide microchannels. After printing, the mold was immersed in IPA to remove uncured HTM140 and subsequently UV

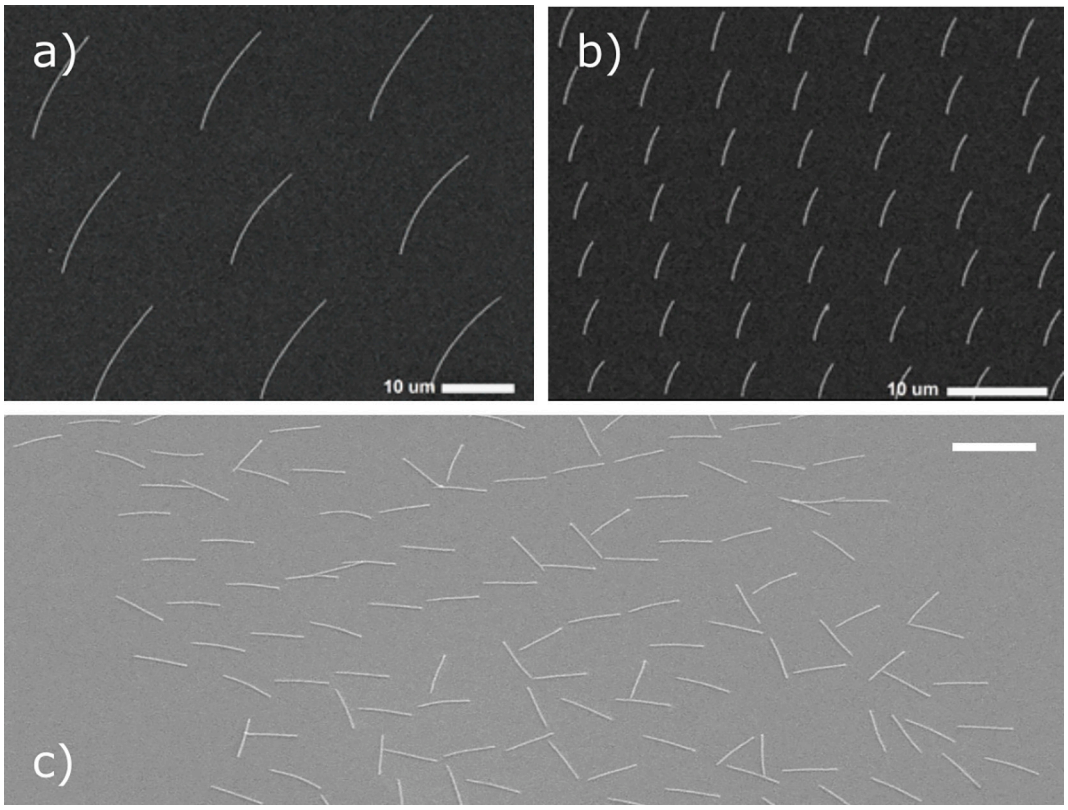

Fig. 3. SEM images of the written nanopillar samples on a 45° sample holder, showing a) maximum aspect ratio of approximately 100, having a pillar diameter of 254 nm ± 17 nm and a height of 25 μm; b) shows the pillar array that was written to mimic the primary cilium in the collecting duct. With a diameter of 251 nm ± 22 nm, a height of 7.5 μm ± 116 nm, and spacing of 8 μm the written cilia do indeed mimic the renal cilia. c) Without critical point drying, the large nanopillars collapse to the substrate during drying due to surface tension forces. All scale bars are 10 μm.

cured (Photopol Curing Unit).

Polydimethylsiloxane (PDMS) elastomer and curing agent (Sylgard 184, Dow Corning) were mixed in a 10:1 ratio, poured in the mold and cured at 70 °C for 1 h. After curing, the PDMS was cut loose with a scalpel around the edges of the master and peeled out. Holes for the inlets and outlets were punched with a 23G blunt-end needle.

The chip was assembled under cleanroom conditions by combining the PDMS component with a glass coverslip that features the nanopillars. PE-10 tubing was inserted in the inlets and outlets and the chip was placed in a custom-made chip holder. This chip holder consisted of a top and bottom part of laser cut transparent acrylate plates held together with four bolts and nuts (M5). With this holder we achieved reversible watertight sealing between the coverslip and PDMS.

3. Results

3.1. Nanopillar arrays

The resolution limit of the 2PP fabrication tool is listed as 200 nm by the equipment manufacturer. We were able to reproducibly achieve pillar arrays with d = 145 ± 4 nm, h = 692 ± 8 nm, and periodicity = 500 nm (i.e. spacing s = 355 ± 4 nm) over an area of 20 μm × 20 μm (Fig. 2a). The optimum scanning speed and laser power were 3 mm/s and 7.5 mW, respectively. The smallest spacing was achieved by writing a nanopillar array with periodicity of 400 nm. This array contained nanopillars with d = 243 ± 8 nm, leading to s = 157 ± 8 nm, with the array measuring 24 μm × 24 μm, achieved with the same scanning speed and laser power as above (Fig. 2b). Both were accomplished using critical point drying to avoid pillar collapse due to capillary forces during drying of the development liquid. Without critical point drying, such dense arrays typically exhibit collapsing pillars, even after using low surface tension development solutions such as Novec 7000 Engineered Fluid (Sigma-Aldrich, Fig. 2c).

The maximum achieved aspect ratio was ~100, for pillars with d = 254 ± 17 nm and h = 25 μm which were written with a scanning speed of 3 mm/s and a laser power of 8 mW (Fig. 3a). Again, pillar arrays underwent critical point drying after development. Without critical point drying, these larger-sized pillars collapsed to the substrate due to surface tension forces of the drying development liquid at the liquid-air interface (Fig. 3c).

When we compare the dimensions of the renal micro-projections with the pillar dimensions we obtained using 2PP, we can clearly see that the primary cilium, located in the collecting duct of the nephron, has dimensions that can easily be reproduced using this technology. A nanopillar array was written with these dimensions to mimic the primary cilia (Fig. 3b). The pillars measured 251 nm ± 22 nm in diameter, 7.5 μm ± 116 nm in height and were spaced at 8 μm. Therefore they mimic the renal cilia, both in terms of morphology and topography (shape and size). 2PP could not, however, be used to fabricate pillars in the small size range of microvilli. The obtained minimum diameter of 145 nm ± 4 nm is almost twice the diameter of a microvillus (80 nm) and the obtained smallest spacing of 157 nm ± 8 nm only approaches the largest spacing we find for a brush border of microvilli (130 nm). The written nanopillar arrays approach but do not match the actual sizes of microvilli. Thus although the surface morphology can be mimicked to some extent, the biological structures are slightly smaller.

Nevertheless, achieving nanopillar arrays with aspect ratios in excess of 100 with individual diameters of ~250 nm is a significant achievement in replicating the morphology and topography of biological environments. As far as the authors are aware, 2PP is one of the only methods capable of achieving such high aspect ratio well-ordered free-standing polymer nanopillars. For replicating microvilli structures, 2PP

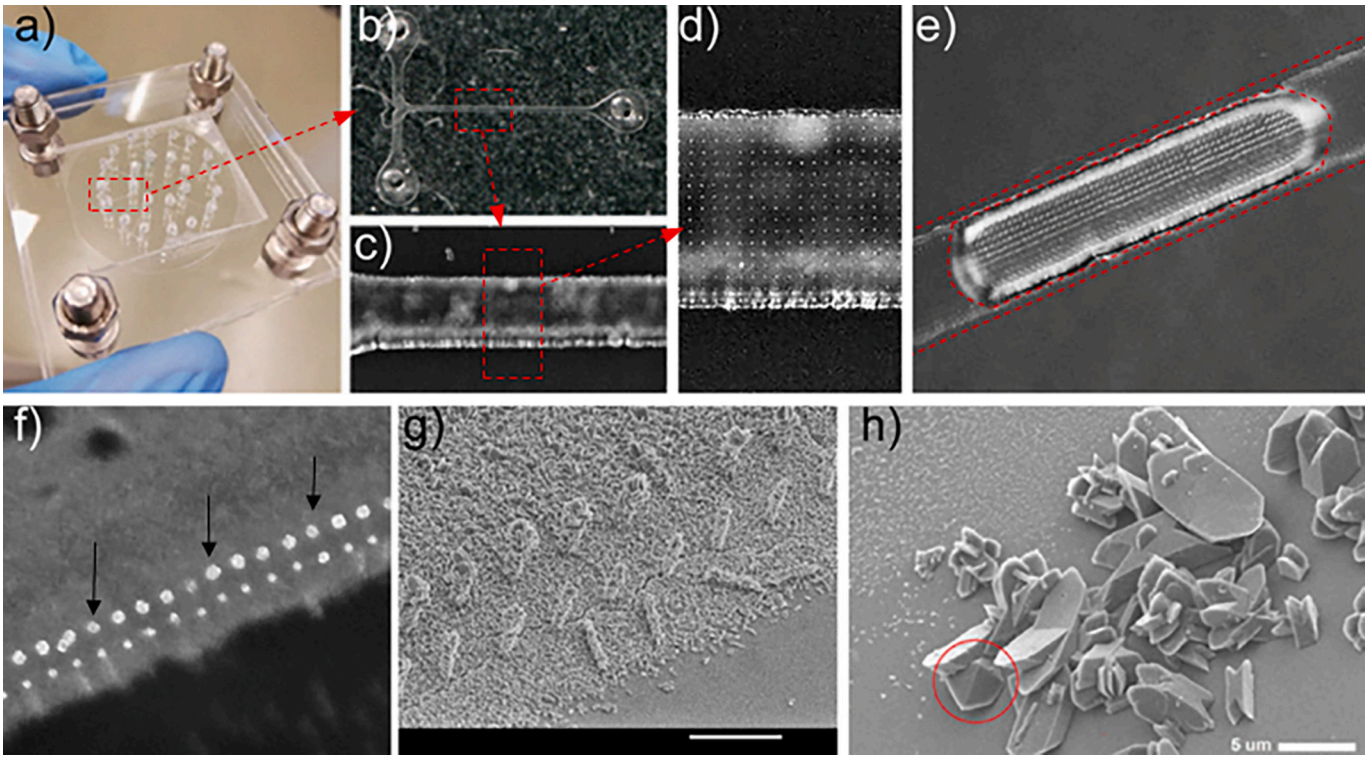

Fig. 4. a) The transparent microfluidic device containing eight microfluidic channels. b) One of the eight microfluidic channels with two inlets and one outlet. The red dotted square indicates the position of the nanopillar array. c) The array of printed cilia inside the microfluidic channel. d) Enlarged region of c) showing printed cilia in detail. e) An air bubble travels through the microchannel, with the walls remaining covered in ethanol. The red dotted line is drawn around the fluid to guide the eye. f) Therefore, pillars and the wall edge do not collapse and crystallization occurs around them, where the bright white points indicated by arrows are the pillars and the light grey area is crystallization of CaOx. g) Crystallization in nanopillar topography within a microfluidic channel under SEM inspection, scale bar = 10 μm. h) CaOx crystals formed in the device after two hours, using calcium and oxalate precursor solutions (8.0 mM) at a flow rate of 1 μL/min. Majority of the crystals is CaOx monohydrate, encircled an individual CaOx dihydrate crystal, scale bar = 5 μm. (For interpretation of the references to colour in this figure legend, the reader is referred to the web version of this article.)

is limited not only by optical contrast and diffraction [38] but also photochemical processes such as diffusion [39]. Feature sizes and, most importantly, gaps between features can only be systematically produced above 200 nm resolution. Further techniques using stimulated depletion [40] or photoresin radical quenching [41] might be ways to improve the size and resolution of such soft matter nano-arrays in a controlled manner. Alternatively, ablation methods such as focussed ion beam can thin down polymer filaments, with some preliminary results showing nanopillar arrays of ~150 nm width, ~150 nm spacing, and ~ 1 μm height. Since these results are at a preliminary stage, they are presented in the Supplementary Information to motivate further efforts in reproducing microvilli topography.

3.2. Microfluidic device

The microfluidic chip consisted of a PDMS component with multiple microchannels closed off with a glass cover slip (Fig. 4a). The nanopillar arrays, written with 2PP on the glass cover slip, were encapsulated by the walls of the microchannels (Fig. 4b, c, and d). The width of those arrays was wider (400 μm) than the width of the microchannel (150 μm) to account for inaccurate positioning. To achieve a watertight seal the microfluidic chip was placed in a transparent chip holder. There was no leakage observed between the PDMS and glass up to a flow rate of 200 μL/min for our channel dimensions given above, which is far above physiological flow rates of typically 1 μL/min [5]. As the surface tension during drying of the pillar arrays caused collapse, filling the chamber with fluid posed the same problem. When the channel was filled with water, the surface tension pushed down the pillars. This was not the case when it was filled with ethanol, which can be explained by its much lower surface tension. The channel was, therefore, first filled with ethanol, then exchanged with water. This made sure the pillars remained upright when the channel was filled with water. However any bubble traveling through the microchannel introduces another liquid-gas phase boundary, where the surface tension again could affect the pillars (Fig. 4e). Therefore the microfluidic setup should be improved with bubble traps to eliminate the introduction of liquid-gas phase boundaries into the channel.

For preliminary experiments and for demonstrating the basic functionality, we used aqueous solutions of calcium chloride ($CaCl_2$, CAS10043–52-4, ≥93.0%, Sigma-Aldrich) and sodium oxalate ($Na_2C_2O_4$, CAS62–76-0, ≥99.5%, Sigma-Aldrich) dissolved in 50 mL of ultrapure water (Elga Purelab, resistivity: 18.2 MΩ·cm at 23.6 °C) in two separate beakers, at 8.0 mM concentration as precursors, and pumped through the microchannel at 1 μL/min for two hours using syringe pumps (Legato 111, KD Scientific) at the two separate inlets shown in Fig. 1 (bottom). Afterwards the chip was demounted, the crystals were examined in an SEM and the crystal phase was determined based on the shape. The majority of crystals was calcium oxalate monohydrate but also individual calcium oxalate di-hydrate crystals were spotted (Fig. 4h). This is an interesting observation as calcium oxalate monohydrate is the more studied form in solubility studies [42] owing to its thermodynamic stability compared to calcium oxalate di-hydrate crystals. The transparent device also enabled us to observe and image a particular microchannel during crystallization. With this, an induction time could be derived. When precursor concentrations were adjusted to mimic physiological concentrations, i.e. 12.0 mM and 0.40 mM for respectively calcium and oxalate precursors [5], we could see crystals forming in the microchannel starting at 165 s. The location of

crystallization was not in the middle of the channel, possibly due to roughness of the microchannel sidewalls or flow inconsistencies from the syringe pumps. These results were, however, too premature for any conclusion and are solely cited as a proof-of-principle.

Nanopillar regions with cilia-type structures were generally found at the edges of the microfluidic channels due to the good wetting of ethanol in these regions (Fig. 4f). Crystallization was also observed in these regions under SEM inspection (Fig. 4g), although pillar collapse was present. Pillar adhesion could be improved via substrate surface treatments such as oxygen plasma, or by increasing the size of the nanopillar at the base. Finally, although critical point drying and rewetting of the microfluidics was necessary in these experiments for proof-of-principle and documenting microstructure integrity along the fabrication process chain, it may be possible to avoid such surface tension collapse effects by keeping the developed microstructures in liquid and clamping them into the microfluidic channel, also in liquid. In this way, since the whole device is kept immersed, no liquid-air transitions occur, with less likelihood of microstructure collapse. Development liquid can then be steadily replaced by, for example, deionized water.

4. Conclusions

We presented a direct fabrication method to fabricate nanopillar arrays mimicking the morphology of surfaces of the cell membrane found in the human nephron. Using two-photon polymerization, we were able to write nanopillars with a minimum diameter of 145 nm $\pm$ 4 nm, nanopillar arrays with a minimum spacing of 157 nm $\pm$ 8 nm and nanopillars with an aspect ratio of up to 100, having a diameter of 254 nm $\pm$ 17 nm and a height of approximately 25 µm. With this we achieved printing of nanopillars that resemble the primary cilia found in the collecting duct of the human nephron. Also we have successfully integrated the printed cilia into a microfluidic chip and crystallized CaOx on that chip. The integration of a microfluidic chip with two-photon polymerization produced surface morphology is a stepping stone towards development of an in vitro organ-on-a-chip technology mimicking kidney stone formation in the human nephron under physiological and dynamic flow conditions.

Our work is now aimed at improving the microfluidic setup with bubble traps and then studying the influence of kidney surface morphology on kidney stone formation. The stochastic nature of crystallization bids us to perform a statistically significant number of experiments to support any claim [43,44]. As there are multiple morphologies found in the nephron, the number of experiments is substantial and time-consuming [45–48]. Our microchip contains eight separate microchannels, which decreases fabrication time. Performing experiments in parallel is expected to decrease the overall experimentation time required to span this substantial parameter space. Finally, given the flexibility of 2PP in creating nanopillars with varying diameters, heights, spacings, and modulus [17], kidney models can be created to study crystallization under a range of surfaces with differing micro-topographies and mechanical behaviours.

Declaration of Competing Interest

The authors declare that they have no known competing financial interests or personal relationships that could have appeared to influence the work reported in this paper.

Acknowledgements

We are pleased to acknowledge valuable discussions with H. Kramer and A. Sharma, and lab support by R. Luttjeboer, H. Jansen, P. van Holst, and S. van Veldhoven. D. F. thanks M. Ganjian for the FIB image.

Appendix A. Supplementary data

Supplementary data to this article can be found online at https://doi.org/10.1016/j.mne.2021.100094.

References

[1] V. Romero, H. Akpinar, D.G. Assimos, Kidney stones: a global picture of prevalence, incidence, and associated risk factors, Rev. Urol. 12 (2–3) (2010) e86–e96.
[2] C.S. Saigal, G. Joyce, A.R. Timilsina, the Urologic Diseases in America Project, Direct and indirect costs of nephrolithiasis in an employed population: opportunity for disease management? Kidney Int. 68 (4) (Oct. 2005) 1808–1814, https://doi.org/10.1111/j.1523-1755.2005.00599.x.
[3] J. Shah, H.N. Whitfield, Urolithiasis through the ages, BJU Int. 89 (8) (Apr. 2002) 801–810, https://doi.org/10.1046/j.1464-410X.2002.02769.x.
[4] A. Tefekli, F. Cezayirli, The history of urinary stones: in parallel with civilization, Sci. World J. 2013 (2013) 1–5, https://doi.org/10.1155/2013/423964.
[5] G. Laffite, et al., Calcium oxalate precipitation by diffusion using laminar microfluidics: toward a biomimetic model of pathological microcalcifications, Lab Chip 16 (7) (2016) 1157–1160, https://doi.org/10.1039/C6LC00197A.
[6] D. Turnbull, Kinetics of heterogeneous nucleation, J. Chem. Phys. 18 (2) (Feb. 1950) 198–203, https://doi.org/10.1063/1.1747588.
[7] Y. Diao, T. Harada, A.S. Myerson, T. Alan Hatton, B.L. Trout, The role of nanopore shape in surface-induced crystallization, Nat. Mater. 10 (11) (Nov. 2011) 867–871, https://doi.org/10.1038/nmat3117.
[8] P. Grosfils, J.F. Lutsko, Impact of surface roughness on crystal nucleation, Crystals 11 (1) (Dec. 2020) 4, https://doi.org/10.3390/cryst11010004.
[9] S. Veesler, F. Puel, Crystallization of pharmaceutical crystals, in: (Eds.), Handbook of Crystal Growth, Elsevier, 2015, p. 915, https://doi.org/10.1016/B978-0-444-56369-9.00021-6.
[10] J.H. Wiessner, A.T. Hasegawa, L.Y. Hung, G.S. Mandel, N.S. Mandel, Mechanisms of calcium oxalate crystal attachment to injured renal collecting duct cells, Kidney Int. 59 (2) (Feb. 2001) 637–644, https://doi.org/10.1046/j.1523-1755.2001.059002637.x.
[11] M.W. Bigelow, J.H. Wiessner, J.G. Kleinman, N.S. Mandel, Calcium oxalate crystal attachment to cultured kidney epithelial cell lines, J. Urol. 160 (4) (Oct. 1998) 1528–1532.
[12] F.L. Coe, A.P. Evan, E.M. Worcester, J.E. Lingeman, Three pathways for human kidney stone formation, Urol. Res. 38 (3) (Jun. 2010) 147–160, https://doi.org/10.1007/s00240-010-0271-8.
[13] S.R. Khan, Heterogeneous nucleation of calcium oxalate crystals in mammalian urine, Scanning Microsc. vol. 9 (2) (Jun. 1995) 597–614, discussion 614–616.
[14] H.H. Arts, N.V.A.M. Knoers, Current insights into renal ciliopathies: what can genetics teach us? Pediatr. Nephrol. 28 (6) (Jun. 2013) 863–874, https://doi.org/10.1007/s00467-012-2259-9.
[15] S. Maruo, O. Nakamura, S. Kawata, Three-dimensional microfabrication with two-photon-absorbed photopolymerization, Opt. Lett. 22 (2) (Jan. 1997) 132, https://doi.org/10.1364/OL.22.000132.
[16] K.-S. Lee, R.H. Kim, D.-Y. Yang, S.H. Park, Advances in 3D nano/microfabrication using two-photon initiated polymerization, Prog. Polym. Sci. 33 (6) (Jun. 2008) 631–681, https://doi.org/10.1016/j.progpolymsci.2008.01.001.
[17] E.D. Lemma, et al., Mechanical properties tunability of three-dimensional polymeric structures in two-photon lithography, IEEE Trans. Nanotechnol. 16 (1) (2016) 23–31, https://doi.org/10.1109/TNANO.2016.2625820.
[18] P. Guo, A.M. Weinstein, S. Weinbaum, A hydrodynamic mechanosensory hypothesis for brush border microvilli, Am. J. Physiol.-Ren. Physiol. 279 (4) (Oct. 2000) F698–F712, https://doi.org/10.1152/ajprenal.2000.279.4.F698.
[19] H. Kojima, A. Ishijima, T. Yanagida, Direct measurement of stiffness of single actin filaments with and without tropomyosin by in vitro nanomanipulation, Proc. Natl. Acad. Sci. 91 (26) (Dec. 1994) 12962–12966, https://doi.org/10.1073/pnas.91.26.12962.
[20] M. Kikumoto, M. Kurachi, V. Tosa, H. Tashiro, Flexural rigidity of individual microtubules measured by a buckling force with optical traps, Biophys. J. 90 (5) (Mar. 2006) 1687–1696, https://doi.org/10.1529/biophysj.104.055483.
[21] D.B. Wells, A. Aksimentiev, Mechanical properties of a complete microtubule revealed through molecular dynamics simulation, Biophys. J. 99 (2) (Jul. 2010) 629–637, https://doi.org/10.1016/j.bpj.2010.04.038.
[22] A.L. Kierszenbaum, Histology and Cell Biology: An Introduction to Pathology, 5th edition, Elsevier Inc, St. Louis, MO, 2019.
[23] K.S. Saladin, C.A. Gan, H.N. Cushman, Anatomy & Physiology: The Unity of Form and Function, Eighth Edition, McGraw-Hill Education, New York, NY, 2018.
[24] H. Sakaguchi, Y. Suzuki, Fine structure of renal tubule cells, Keio J. Med. 7 (1958) 17–37, https://doi.org/10.2302/kjm.7.17.
[25] S. Weinbaum, P. Guo, L. You, A new view of mechanotransduction and strain amplification in cells with microvilli and cell processes, Biorheology 38 (2–3) (2001) 119–142.
[26] H. Hücker, H. Frenzel, Scanning electron microscopy of the distal nephron and calyx of the human kidney, Virchows Arch. B Cell Pathol. 18 (2) (1975) 157–164, https://doi.org/10.1007/BF02889244.
[27] J. Gorelik, et al., Dynamic assembly of surface structures in living cells, Proc. Natl. Acad. Sci. 100 (10) (May 2003) 5819–5822, https://doi.org/10.1073/pnas.1030502100.

[28] J.A. Deane, S.D. Ricardo, Emerging roles for renal primary cilia in epithelial repair, in: International Review of Cell and Molecular Biology vol. 293, Elsevier, 2012, pp. 169–193, https://doi.org/10.1016/B978-0-12-394304-0.00011-7.
[29] V. Raghavan, O.A. Weisz, Discerning the role of mechanosensors in regulating proximal tubule function, Am. J. Physiol.-Ren. Physiol. 310 (1) (Jan. 2016) F1–F5, https://doi.org/10.1152/ajprenal.00373.2015.
[30] B. Kaissling, S. Bachmann, W. Kriz, Structural adaptation of the distal convoluted tubule to prolonged furosemide treatment, Am. J. Physiol.-Ren. Physiol. 248 (3) (Mar. 1985) F374–F381, https://doi.org/10.1152/ajprenal.1985.248.3.F374.
[31] G.K. Kumaran, I. Hanukoglu, Identification and classification of epithelial cells in nephron segments by actin cytoskeleton patterns, FEBS J. 287 (6) (Mar. 2020) 1176–1194, https://doi.org/10.1111/febs.15088.
[32] H. Oberleithner, B. Schmidt, P. Dietl, Fusion of renal epithelial cells: a model for studying cellular mechanisms of ion transport, Proc. Natl. Acad. Sci. 83 (10) (May 1986) 3547–3551, https://doi.org/10.1073/pnas.83.10.3547.
[33] D. Fan, "Unpublished data".
[34] D. Tan et al., "Reduction in feature size of two-photon polymerization using SCR500," Appl. Phys. Lett., 90, 7, p. 071106, Feb. 2007, https://doi.org/10.1063/1.2535504.
[35] M. Emons, K. Obata, T. Binhammer, A. Ovsianikov, B.N. Chichkov, U. Morgner, Two-photon polymerization technique with sub-50 nm resolution by sub-10 fs laser pulses, Opt. Mater. Exp. 2 (7) (Jul. 2012) 942, https://doi.org/10.1364/OME.2.000942.
[36] K. Takada, H.-B. Sun, S. Kawata, Improved spatial resolution and surface roughness in photopolymerization-based laser nanowriting, Appl. Phys. Lett. 86 (7) (2005) 071122, https://doi.org/10.1063/1.1864249.
[37] S. Kawata, H.-B. Sun, T. Tanaka, K. Takada, Finer features for functional microdevices, Nature 412 (6848) (Aug. 2001) 697–698, https://doi.org/10.1038/35089130.
[38] J. Fischer, M. Wegener, Three-dimensional optical laser lithography beyond the diffraction limit: 3D optical lithography off limits, Laser Photonics Rev. 7 (1) (Jan. 2013) 22–44, https://doi.org/10.1002/lpor.201100046.
[39] N. Uppal, Modeling of temperature-dependent diffusion and polymerization kinetics and their effects on two-photon polymerization dynamics, J. MicroNanolithogr. MEMS MOEMS 7 (4) (Oct. 2008) 043002, https://doi.org/10.1117/1.3033203.
[40] R. Wollhofen, J. Katzmann, C. Hrelescu, J. Jacak, T.A. Klar, 120 nm resolution and 55 nm structure size in STED-lithography, Opt. Express 21 (9) (May 2013) 10831, https://doi.org/10.1364/OE.21.010831.
[41] S.H. Park, T.W. Lim, D.-Y. Yang, R.H. Kim, K.-S. Lee, Improvement of spatial resolution in nano-stereolithography using radical quencher, Macromol. Res. 14 (5) (Oct. 2006) 559–564, https://doi.org/10.1007/BF03218724.
[42] F. Ibis, P. Dhand, S. Suleymanli, A.E.D.M. van der Heijden, H.J.M. Kramer, H. B. Eral, A combined experimental and modelling study on solubility of calcium oxalate monohydrate at physiologically relevant pH and temperatures, Crystals 10 (10) (Oct. 2020) 924, https://doi.org/10.3390/cryst10100924.
[43] A.M. Kolbach-Mandel, J.G. Kleinman, J.A. Wesson, Exploring calcium oxalate crystallization: a constant composition approach, Urolithiasis 43 (5) (Oct. 2015) 397–409, https://doi.org/10.1007/s00240-015-0781-5.
[44] D.J. Kok, S.E. Papafoulos, L.J.M.J. Blomen, O.L.M. Bijvoet, Modulation of calcium oxalate monohydrate crystallization kinetics in vitro, Kidney Int. 34 (3) (Sep. 1988) 346–350, https://doi.org/10.1038/ki.1988.187.
[45] P. Laval, N. Lisai, J.-B. Salmon, M. Joanicot, A microfluidic device based on droplet storage for screening solubility diagrams, Lab Chip 7 (7) (2007) 829, https://doi.org/10.1039/b700799j.
[46] B. Zheng, L.S. Roach, R.F. Ismagilov, Screening of protein crystallization conditions on a microfluidic chip using nanoliter-size droplets, J. Am. Chem. Soc. 125 (37) (Sep. 2003) 11170–11171, https://doi.org/10.1021/ja037166v.
[47] Y. Ai, R. Xie, J. Xiong, Q. Liang, Microfluidics for biosynthesizing: from droplets and vesicles to artificial cells, Small 16 (9) (Mar. 2020) 1903940, https://doi.org/10.1002/smll.201903940.
[48] T. Nisisako, T. Torii, T. Higuchi, Droplet formation in a microchannel network, Lab Chip 2 (1) (2002) 24–26, https://doi.org/10.1039/B108740C.